



Nano-size IrO_x catalyst of high activity and stability in PEM water electrolyzer with ultra-low iridium loading



Haoran Yu^{a,b,*}, Nemanja Danilovic^{c,1}, Yang Wang^d, William Willis^e, Abhinav Poozhikunnath^d, Leonard Bonville^b, Chris Capuano^c, Katherine Ayers^c, Radenka Maric^{a,b}

^a Department of Chemical and Biomolecular Engineering, University of Connecticut, 191 Auditorium Road, Unit 3222, Storrs, CT, 06269-3222, USA

^b Center for Clean Energy Engineering, University of Connecticut, 44 Weaver Road Unit 5233, Storrs, CT, 06269-5233, USA

^c Proton OnSite, 10 Technology Drive, Wallingford, CT, 06492, USA

^d Department of Material Science and Engineering, University of Connecticut, 97 North Eagleville Road, Storrs, CT, 06269-3136, USA

^e Department of Chemistry, University of Connecticut, 97 North Eagleville Road, Storrs, CT, 06269-3061, USA

ARTICLE INFO

Keywords:

Proton exchange membrane water electrolysis
Iridium oxide
Reactive spray deposition technology
Oxygen evolution reaction
Stability

ABSTRACT

The balance of catalyst loading, activity and stability remains a challenge for the anode of proton exchange membrane (PEM) water electrolyzers. Here we report a nano-size IrO_x/Nafion® composite catalyst that exhibits both outstanding activity for oxygen evolution reaction (OER) and stability in a PEM water electrolyzer. The IrO_x/Nafion® catalyst layer is fabricated using a flame-based cost-effect process, reactive spray deposition technology. The IrO_x/Nafion® catalyst shows > 10 times improvement in OER mass activity compared to IrO_x nanoparticles synthesized using the wet chemistry method. The IrO_x/Nafion® catalyst also achieved ~4,500 h of stable operation in MEA electrolyzer at 1.8 A cm⁻² and 80 °C with ultra-low iridium loading of 0.08 mg cm⁻². Analysis of the IrO_x structure and the electrochemical performance revealed three key factors for balancing high stability and activity: (1) high ratio of Ir (IV) to Ir (III) species and high content of hydroxide on the surface; (2) high anodic charge and surface area due to nano-size IrO_x particles that are well-dispersed in the Nafion® ionomer electrolyte; (3) homogeneous anode catalyst layer morphology.

1. Introduction

Hydrogen production by water electrolysis in water electrolyzers (WEs) has been developed as an alternative technology for energy conversion and storage that is well-integrated into the electric grid of renewable energy systems [1–6]. However, with current methods, hydrogen produced by electrolysis is more expensive than hydrogen produced by other technologies. Therefore, water electrolysis accounts for a mere 4% of the global hydrogen production and the rest of production sources are all related to fossil fuels [1]. Hydrogen that is produced in electrolysis will only be competitive when the cost is reduced and the stability is improved [7].

Proton exchange membrane (PEM) water electrolysis systems offer several advantages over traditional electrolysis technologies [8–11] and has the potential to be the most cost-effective on a large scale. But significant advances are needed in catalyst and membrane materials as well as in the labor-intensive manufacturing process. The state-of-the-art anode catalysts in conventional proton exchange membrane water

electrolyzers (PEMWES) are iridium oxide or mixed oxide with ruthenium [12,13]. Typical catalysts for commercial electrodes have iridium oxide loading from 1 to 3 mg cm⁻² [14]. This level of catalyst loading is too high to meet the long term cost targets for energy markets [13,15,16]. Furthermore, while using current electrolysis technology, the translation of catalyst development from lab scale to the megawatt scale remains challenging in terms of catalyst cost and stability [15].

The enhancement of catalyst stability is of equal importance as the reduction of catalyst loading. Long-term operation at high current density up to thousands of hours is particularly challenging with an Ir loading less than 1 mg cm⁻². Recent literature has seen a growing number of studies on longer-term electrolysis operation ranging from hundreds to several thousand hours [17–24]. The best reported stability was on a nano-structured thin film (NSTF) cell which achieved 5,000 h with a constant current load of 2 A cm⁻² and 0.25 mg cm⁻² Ir loading [17]. Iridium oxide supported on Ti catalyst with 50 wt. % Ir and a low catalyst loading of 0.12 mg cm⁻² achieved more than 1,000 h of operation at a lower current load of 1 A cm⁻² [23]. No supported catalyst,

* Corresponding author at: Center for Clean Energy Engineering, University of Connecticut, 44 Weaver Road Unit 5233, Storrs, CT, 06269-5233, USA.
E-mail address: haoran.yu@uconn.edu (H. Yu).

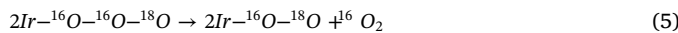
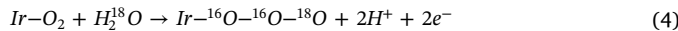
¹ Present address: Lawrence Berkeley National Laboratory, 1 Cyclotron Road, Berkeley, CA 94720 USA.

other than titanium-supported catalysts, has been able to achieve such high catalyst stability [25].

Achieving catalyst loading reduction and stability improvement requires an understanding of the mechanisms for oxygen evolution reaction (OER). Several OER mechanisms have been proposed for iridium oxide and a unified theory has yet to be established. In one mechanism, the O–O bond forms via two adsorbed oxygen atoms on two iridium sites, thus termed binuclear mechanism. Based on the early work of Bockris [26], the OER on iridium oxide electrode follows the reaction path below [27]:

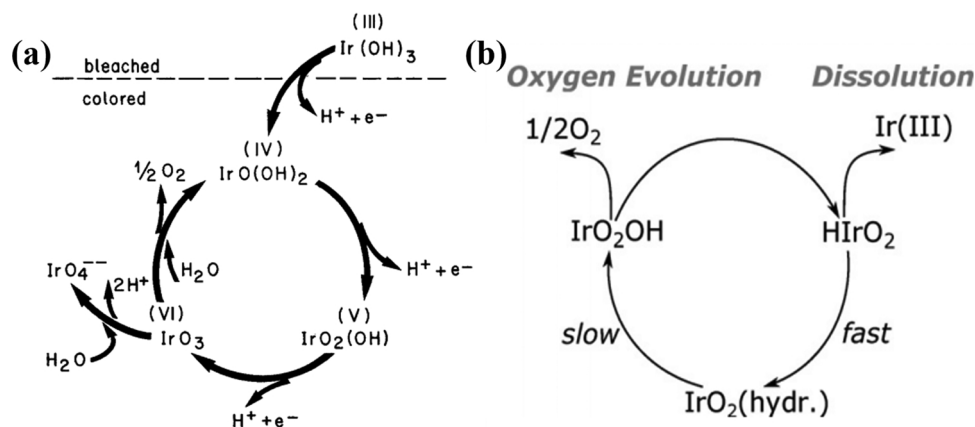


The second step is the (Rate determining step) RDS resulting a Tafel slope of 40 mV/dec. which agrees with experimental results [27]. Partial evidence for this pathway is provided by oxygen isotope labeling [28] where lattice oxygen is participating in the OER:

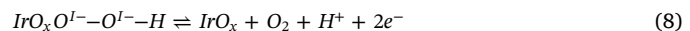
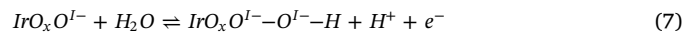
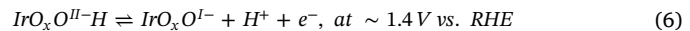


Kotz, et al. [29] attempted to characterize sputtered iridium electrode at various anodic potentials by fast insertion into the electron spectrometer. Although Ir (III) and Ir (IV) hydroxide are observed (Scheme 1a), higher iridium oxidation states (V and VI) lack evidence in that work [29]. Recent studies on amorphous iridium oxide includes the participation of Ir (III) species and the Ir (III) and Ir (IV) intermediates are experimentally confirmed with X-ray absorption spectroscopy (XAS) and X-ray photoelectron spectroscopy (XPS) [30–37]. The presence of Ir (III) species and high iridium hydroxide content are crucial for achieving higher activity than rutile IrO_2 . Following this argument, Cherevko et al., [38] proposed a cyclic reaction pathway (Scheme 1b) that composed of lower iridium oxidation states (III, IV and V) than Kotz, et al. [29]. Since the transition from IrO_2 hydroxide (IV) to IrO_2OH (V) is RDS (Scheme 1b), the Tafel slope for this pathway is also 40 mV/dec., confirmed experimentally by [33,34,37–40].

Combining multiple spectroscopic studies of amorphous iridium oxide at OER potentials, Pfeifer and coworkers [31,32,35,36,40] developed another OER scheme involving O–O bond formation through the nucleophilic attack of the electrophilic oxygen (O^{1-}) species in the Ir (III/IV) oxohydroxides. The origin of oxidation signal at about 1.4 vs. RHE in the cyclic voltammetry (CV) of iridium oxide is attributed to the formation of O^{1-} species, rather than the oxidation of Ir (IV) to Ir (V). Thus, the following reaction path is suggested [32]:



Scheme 1. Oxygen evolution circle of reactions proposed by Kotz, et al. [29] (Reprinted with permission from Electrochemical Society.) and Cherevko et al. [38]. (Reprinted with permission from Elsevier.).



It is noted that IrO_x represents the Ir (III/IV) oxohydroxides. It is unclear in this mechanism whether oxygen evolves from single or double iridium sites and no Tafel slopes are reported for this mechanism.

The third OER mechanism is a mononuclear path proposed based on a DFT calculation on the (110) surface of a rutile-type oxide [41,42]. Water dissociation occurs on a single metal site to form the adsorbed O^\cdot -species. The O–O bond forms when a second water molecule dissociates on the same site ($\cdot\text{OOH}$). This pathway can be summarized below [42,43]:



For rutile IrO_2 , the formation of O^\cdot in the second step requires the highest activation energy and is the RDS [43,44]. The mononuclear path has been successful in predicting OER activity of different metal oxides using the binding energy of O^\cdot species as a descriptor [42,44,45]. In addition, the mononuclear path assumes a coupling of electron and proton transfer at each step. This results in a pH-independent behavior [13] and agrees with the results reported in [43,46,47]. Further, Casalongue et al. [48] carried out in situ observations of iridium oxide surfaces using XPS and provide evidence for reaction (5) with observed surface Ir (V) intermediate species. However, the iridium oxidation states during OER are still debated. Pfeifer et al. [40] challenged that the Ir (V) species observed in [48] should be Ir (III) species using XPS and XAS results coupled with DFT modeling. Despite being supported by numerous studies, the DFT model, on which the mononuclear path is based, represents a necessary but not a sufficient analysis of the OER mechanism because it only considers thermodynamics and does not account for kinetic barriers [42].

In the present work, we use the model from Pfeifer et al. [40] to analyze the XPS results, and a good fit with experimental data is obtained suggesting the presence of a mixed Ir (III)/Ir (IV) surface with high hydroxide content for IrO_x nanoparticles. In addition, the Tafel slopes obtained from rotating disk electrode (RDE) measurements are 40–45 mV/dec. which is close to the results presented in [27] and [33]. Therefore, the discussion of OER activity and catalyst stability are based

Table 1
Summary of flame conditions.

Flame condition	Ir precursor flow rate (mL min ⁻¹)	Ir precursor concentration (mM)	Oxygen flow rate (SLPM)	Air quench distance (cm)	Air quench flow rate (SLPM)
F1	5	10	8	14	83
F2	8	12.5	12	15.24	130

on the binuclear mechanism.

In summary, the evidence for Ir (V) or higher oxidation states in the binuclear mechanism are still lacking in the literature. However, the presence of Ir (III) and Ir (IV) during OER are confirmed experimentally and a consensus is reached regarding higher OER activity for amorphous iridium oxide than that for rutile-IrO₂. This brings up the question of which oxide is more stable. The balance between activity and stability for Ir-based OER catalysts has been reported [49,50] which strongly depends on the chemical nature of the oxide and its surface properties [13]. Since it is known that the oxide properties are highly sensitive to synthesis conditions, most synthesis methods involve a calcination step to improve the catalyst's stability [27,33,34,51–54]. Experimental results show that thermally prepared iridium oxide has higher stability against dissolution but lower activity compared to amorphous iridium oxide [34,51,54]. The study of iridium dissolution was first reported by Buckley and Burke [55], where a Tafel relation was found between the dissolution rate vs. anodic potential. The Tafel slopes of dissolution and OER in the same potential window are both close to 60 mV/dec. and thus a shared intermediate between OER and iridium dissolution was postulated [55]. This hypothesis is also recognized by Cherevko and coworkers [34,38,52,56] who propose that iridium dissolution and OER are two pathways sharing an intermediate species, Ir (III) (Scheme 1b). A recent study from the same group [57] identified three possible pathways of iridium dissolution based on online electrochemical mass spectroscopy (OLEMS) studies, which are (1) direct dissolution of metallic iridium; (2) through Ir (IV)-Ir(III) transition; (3) and formation of IrO₃ at high potentials. The latter two pathways share a common Ir (III) intermediate with OER. Thus, it is possible that the low stability of amorphous iridium oxide could be due to the high Ir (III) content. But no direct evidence regarding the dissolved iridium species has been reported yet.

The objective of the present study is to synthesize highly active and highly stable anode catalysts by utilizing a flame-based cost-effective process, reactive spray deposition technology (RSDT). The RSDT process offers unique synthesis conditions where IrO_x particles are formed from a fast decomposition of precursor and undergo a rapid calcination step at extremely high temperature 1700–2000 °C [58,59]. The calcination step is immediately followed by an air-quenching step which allows for controlling the residence time of IrO_x particle in the calcination zone. After the IrO_x particles are formed, the Nafion® ionomer is incorporated to form the anode catalyst layer. In this study, we demonstrate the capability of fabricating both the anode and cathode catalyst layers with scaled-up active area using the RSDT process. Details on cathode fabrication and optimization can be found in our previous publication [60]. The OER activity, long-term electrolysis stability and the structural properties of IrO_x particles produced with two synthesis conditions are studied. Additionally, the effect of anode catalyst layer morphology on long-term stability is investigated.

2. Experimental

2.1. Chemicals and materials

Iridium and platinum acetylacetone (Colonial Metals, Inc) were used as the precursor for the anode and cathode deposition, respectively. The iridium precursor was dissolved in a combination of

diethylene glycol monobutyl-ether (Fisher Scientific, laboratory grade), ethanol (Fisher Scientific, anhydrous histological grade) and xylene (Sigma Aldrich, ACS reagent, ≥ 98.5%) with 1:1:2 vol ratio at 10 or 12.5 mM iridium concentration. The Pt precursor was dissolved in a combination of 75 wt. % xylene and 25 wt. % acetone (Sigma Aldrich, HPLC ≥ 99.9%) at 10 mM platinum concentration. Liquid propane (Airgas, Inc., 90%) was added to the precursor solutions at 16 wt. % prior to deposition to aid atomization and increase the combustion heat during the RSDT process.

Nafion® (5 wt. %, 1100 EW, Ion Power, Inc.) was used as the binder for the anode catalyst layer. The Nafion® solution was prepared by adding the 5 wt. % solution drop-wise into methanol. The concentration of Nafion® (mg mL⁻¹) was calculated based on the amount of solid polymer in the solution. The Nafion® solution was stirred continuously for at least 30 min prior to use. Vulcan XC-72R (Cabot Corp.) carbon black was used as the catalyst support for the cathode. The carbon black was dispersed in methanol at a concentration of 2.5 mg mL⁻¹ and Nafion® was used as the binder. The Nafion®/carbon weight ratio was kept at 0.15. The slurry was sonicated (Misonix S-4000, QSonica, LLC, Newton CT) for 180 min in an ice bath prior to use. Nafion® N117 membrane (175 μm thickness, 1100 EW) was used as the electrolyte membrane for the electrolyzer cell.

2.2. Preparation of catalyst-coated membrane

Catalyst-coated membranes (CCM) were fabricated in a one-step process using RSDT [61]. Catalyst was deposited directly on the dry N117 membrane. During anode catalyst layer optimization, two sets of flame conditions were used to synthesize the IrO_x particles (Table 1). The air quench flow rate was adjusted so that the substrate temperature remained in the range of 100–120 °C. Additionally, two spraying conditions were used for the Nafion® solution with different concentrations and flow rates (Table 2). Diluted Nafion® solution was sprayed using two 781S-46 F air-assisted nozzles (EFD, Inc., East Providence, RI) mounted at 180° following the quench. Note that the flow rates in Table 2 refer to the total flow rate from the two nozzles combined.

Table 3 summarizes the key samples for the anode optimization. Cell-1, 2 and 3 were coupled with a Pt-black GDE on the cathode (3 mg_{Pt} cm⁻²) provided by Proton OnSite. Cell-4 and 5 were fully fabricated CCMs using only the RSDT process. It should be noted that the great discrepancy of Ir loading between Cell-2 and Cell-3 was due to the changes on Nafion® spray condition and the removal of large surface agglomerates. These will be discussed in detail in the results and discussions section.

To prepare the samples for electrochemical measurement using RDE, the deposition time was 45 min and 30 min with condition F1 and F2, respectively, resulting an Ir loading of 20 ± 5 μg cm⁻². The Nafion® spray followed N2 condition to reduce the surface agglomerates. The catalyst thin films were deposited directly onto the gold disk inserts (5 mm OD, Pine Instruments Inc.). Two samples were made simultaneously in the deposition for each condition; and the average value obtained from the two samples was used to express the OER activity and the related confidence range (± 11–15%).

For CCMs fabricated fully with RSDT process, the anode condition followed flame condition F2 and Nafion® spray condition N2 which showed the best MEA durability (Table 3). To further improve the stability, the iridium loading of Cell-5 was increased to 0.08 mg cm⁻².

Table 2
Summary of conditions for Nafion® solution spray.

Nafion® spray condition	Flow rate (mL min ⁻¹)	Nafion® concentration (mg cm ⁻²)
N1	2.1	0.4
N2	1.5	0.3

Table 3

Summary of sample specifications for anode catalyst layer.

Sample ID	Sample configurations	Flame condition	Nafion® spray condition	Deposition time (min)	CCM Active area (circular, cm ²)	Anode catalyst layer thickness ^a (μm)	Iridium loading ^b (mg cm ⁻²)
Cell-1	RSDT anode/Proton Pt-black cathode	F1	N1	180	28	1-1.5	0.2 ± 0.03
Cell-2	RSDT anode/Proton Pt-black cathode	F2	N1	180	28	2-2.2	0.4 ± 0.04
Cell-3	RSDT anode/Proton Pt-black cathode	F2	N2	55	28	1.4-1.7	0.037 ± 0.005
Cell-4	RSDT anode/RSDT cathode	F2	N2	55	28	1.5-1.7	0.04
Cell-5	RSDT anode/RSDT cathode	F2	N2	165	86	2-2.5	0.08

^a Range measured from cross-sectional SEM images.^b Obtained from inductively coupled plasma (ICP) analysis.

Furthermore, Cell-5 demonstrated the scaled-up activation area design with an active area of 86 cm². The cathode fabrication conditions followed the same process as in reference [60] with platinum loading of 0.3 ± 0.03 mg cm⁻².

2.3. Physical characterizations

The surface morphology and electrode thickness were characterized by Teneo (Thermo Scientific) scanning electron microscopy (SEM) with a field emission source and Everhart-Thornley (secondary electron) detector. Micrographs of transmission electron microscopy (TEM) were obtained by Tecnai T12 (Thermo Scientific) with a LaB₆ source at 120 keV. High-resolution TEM images were obtained by Talos TEM (Thermo Scientific) with a field emission source at 200 keV. The TEM specimens for individual IrO_x particles were prepared by directly collecting from the flame process for 45 s, without spraying the Nafion® solution. The TEM specimen for IrO_x/Nafion® agglomerates were prepared by scrapping off the as-deposited thin film from a Teflon substrate. The scrapped-off powder was sonicated in ethanol for 30 min and pipetted on to a Cu TEM grid. Then, the TEM grid was dried under ambient air at room temperature for 12 h. The particle size distribution was identified using ImageJ software. A total of 2500 and 2900 particles were used to determine the particle size distribution of F1 and F2 samples, respectively. The iridium and platinum loading of the deposited films was determined by inductively coupled plasma optical emission spectroscopy (ICP-OES) using a Perkin Elmer Optima 7300DV ICP-OES. XPS was obtained using a Phi 510 X-ray Photoelectron Spectrometer (radiation source: Al K α , $\lambda = 1486.6$ eV) to examine the surface iridium composition. The binding energies reported in this study were charge-corrected to obtain the adventitious carbon 1 s binding energy of 284.8 eV. The XPS data were processed with CASA-XPS software. Post-test analysis of the MEA is performed using high-angle annular dark field (HAADF) images and X-ray energy dispersive spectroscopy (XEDS) mapping obtained with the Talos TEM. The TEM specimen was prepared with a focused-ion beam (FIB) lift-out technique [62].

2.4. Electrochemical measurements

Electrochemical measurements were conducted using a custom designed three-compartment electrochemical cell (Adams & Chittenden Scientific Glass, CA). The electrochemical cell was surrounded by a water-jacketed sheath with the water temperature thermo-equilibrated at 25 °C (Isotemp 3016D, Fisher). Nitrogen-purged 0.1 M perchloric acid (double distilled, GFS Chemicals, Inc.) was used as the electrolyte. The potential was determined using Hg/HgSO₄ reference electrode with a potential of 0.72 V vs. RHE. A Pt flag was used as the counter electrode. The working electrode was mounted on an MSR rotator (AFMSRCE, Pine Instruments). An AutoLab PGSTST302 N potentiostat was used for all measurements. Prior to the measurement, the working

electrode underwent electrochemical cleaning by cycling between 0.0 V and 1.5 V (vs. RHE) at a scan rate of 200 mV s⁻¹ for 40 cycles. The quasi-stationary polarization curves for OER was recorded from 1.45 to 1.69 V vs. RHE with a step size of 20 mV and dwell time of 5 min at each potential [63]. The performance was recorded with a rotation speed of 1600 rpm. The high frequency resistance (HFR) was measured using electrochemical impedance spectroscopy (EIS) after each step of chronoamperometry. Cyclic voltammograms (CVs) were collected in nitrogen-purged cell between 0.0 V and 1.4 V (vs. RHE) at a scan rate of 20 mV s⁻¹ for 30 cycles until repeatable and the last cycle was shown. It is noted that the higher potential region was not tested for the quasi-stationary polarization because the accumulated bubbles could not be removed effectively at 1600 rpm. Bubble formation and oxygen oversaturation can introduce mass transport resistance at high current densities. [64] Thus, the upper potential range was determined such that the highest current density do not exceed 10 mA cm⁻². [63]

2.5. Stability testing and scale-up demonstration

The membrane electrode assemblies (MEAs) were assembled and tested at Proton OnSite. Stability testing was conducted by applying a constant current density of 1.8 A cm⁻² and hydrogen pressure of 2.76 MPa (400 psi) while monitoring the change of the cell potential over time. Proton's commercially available PEM electrolyzer stack (28 cm²) hardware was used for MEA testing. This cell stack architecture provides a test bed representative of typical conditions an electrode would experience during standard operation, including differential pressure. Automatic data acquisition was also incorporated to monitor and record operating parameters. Scale-up operation was based on Proton's 86 cm² cell stack hardware with the same operational capability as the 28 cm² apparatus. The baseline configurations used as the reference consisted of an Ir/IrO₂ catalyst (3 mg cm⁻²) and Pt-black (3 mg cm⁻²) catalyst directly deposited onto gas diffusion layers (GDL) with an air brush. DuPont's 7-mil Nafion® membrane (N117) was used as the electrolyte membrane for all cells tested.

3. Results and discussions

3.1. Microstructure of IrO_x/Nafion® catalyst layer

The TEM micrographs of IrO_x particles with flame condition F1 and F2 are presented in Figs. 1(a,b) and 2 (a,b), respectively. To produce images of the individual IrO_x particles, the TEM specimen was deposited for 45 s and no Nafion® solution was co-sprayed with the iridium precursor. The IrO_x particle size distribution was similar for the two flame conditions with an average volume/area particle size ($d_{v/a}$) [65] of 1.9 ± 0.1 nm. The TEM micrographs of IrO_x/Nafion® agglomerates are shown in Figs. 1(c,d) and 2(c,d). The IrO_x/Nafion® agglomerates were mostly spherical with diameters of 10–30 nm. The Nafion® ionomer serves as the electrolyte in which the IrO_x particles are

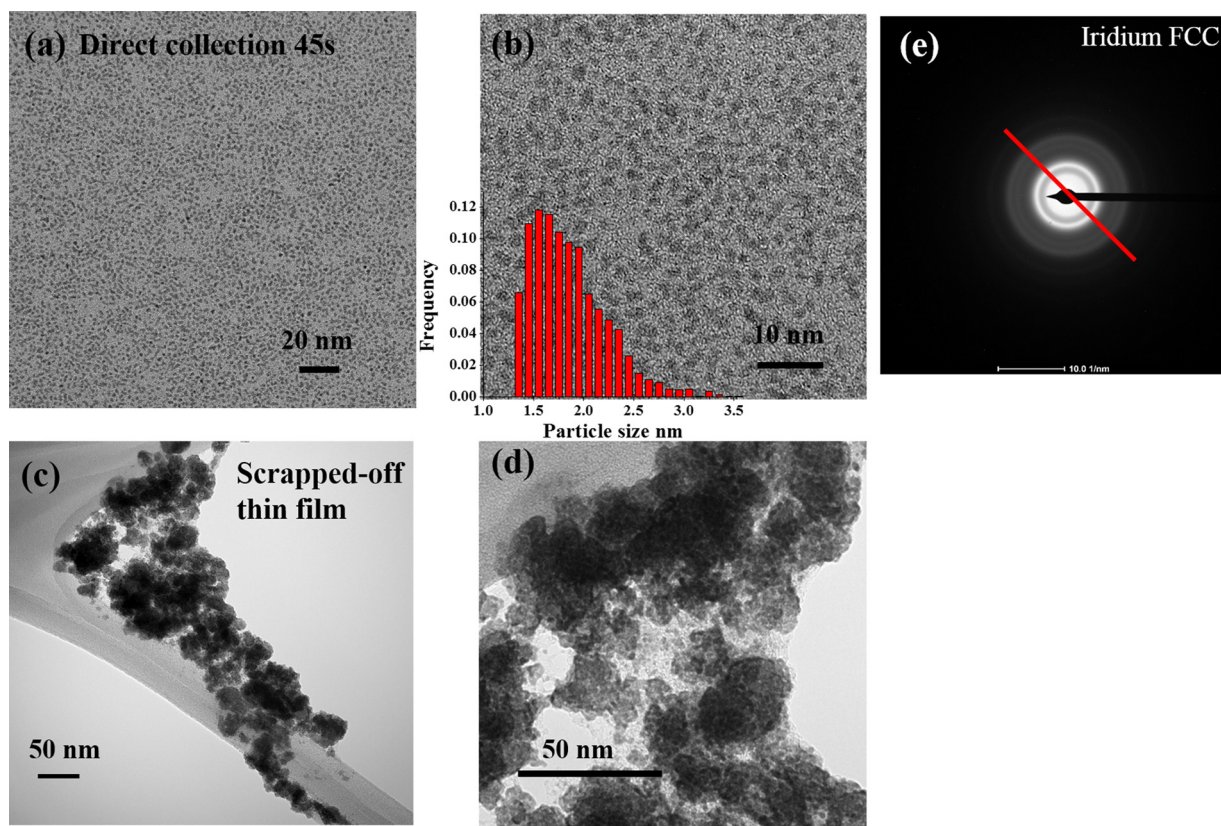


Fig. 1. (a, b) Bright field TEM images on IrO_x particles deposited with F1 condition. The Nafion® slurry were not co-sprayed with the iridium precursor. A total of ~2500 particles were included to derive the particle size distribution histogram. (c, d) The IrO_x/Nafion® agglomerates deposited with condition F1 and N1. (e) The electron diffraction pattern of (a) with a line to show where the intensity profile is determined to measure the d spacing.

embedded and allows the transport of water and protons to the IrO_x particles. Individual IrO_x particles can be distinguished in Figs. 1d and 2d, indicating a good dispersion of the IrO_x particles in the ionomer. However, the majority of IrO_x particles in the agglomerates are heavily overlapped and thus it is difficult to obtain a particle size distribution from Figs. 1(c,d) and 2(c,d). In this work, the IrO_x particle size distribution with or without ionomer are considered identical as the IrO_x particle size depends primarily on the flame condition.

It is noted that TEM images (Figs. 1 and 2) do not reveal the true structure of the as-deposited nanoparticles. The purpose of TEM images is only to analyze the particle size distribution. The oxidation state of iridium is determined from XPS using the fitting model proposed in [40] which will be discussed in the following sections. Therefore, lattice fringes or electron diffraction patterns are not used to determine the crystal structure of the nanoparticles in this work. This is due to the concern that the electron beam could reduce the IrO_x nanoparticles and the particles could be coarsened after extended exposure. Thus, all images were taken quickly and at a fresh location of the specimen. The lattice fringes show a mixture of Ir (111) and IrO₂ (101) planes (Fig. 2b). The d spacing is measured from electron diffraction pattern (Figs. 1e and 2e) using the intensity profile along the line. Five such lines are used to determine the average d spacing. The diffraction patterns exhibit FCC structure from metallic iridium (Table 4). Similar issues with TEM characterization were reported in [66].

To gain further understanding of the formation of IrO_x particles in the flame, a simple model is proposed to estimate the IrO_x particle size. It is assumed that the precursor solution can be approximated to an ideal mixture so that Raoult's law and Dalton's law can be applied. In the RSDT process, the precursor stream is atomized into droplets in the range of 3–60 μm diameter [58], followed by flame combustion. Fig. 3(a) shows the force diagram of a single droplet. The critical droplet size can be obtained when the internal force (F_{downward}) is balanced

by the surface tension (F_{upward}). Thus, the critical droplet size is calculated by:

$$\Delta P = P_i - P_0 = \frac{2\sigma}{r_{\text{critical}}} \quad (14)$$

P_i represents the internal pressure of the droplet. P_0 is the ambient pressure. σ is the surface tension of the droplet. r_{critical} is the critical radius of the particle. It is hypothesized that the pressure difference (ΔP) equals to the vapor pressure of the mixed solvents. The calculated critical droplet sizes are shown in Fig. 3b as a function of droplet temperature. The critical droplet size is in the range of 20–200 nm which is much smaller than the droplet size exiting the nozzle. This suggests that the droplets are fragmented until the droplet size is equal or less than the critical size. The corresponding IrO_x particle size is calculated in Fig. 3b. The IrO_x particle size is in the range of 1–10 nm. The experimentally observed 1.5–2 nm size range corresponds to a droplet temperature of 80–90 °C, in reasonable agreement with the measured nozzle temperature of 60–70 °C. This indicates that the droplets are gently heated up during fragmentation. Additionally, the change of iridium precursor concentration shows minor influence on the IrO_x particles, especially at temperatures higher than 60 °C. The IrO_x particle size is decreased by 7% when changed from F2 to F1 condition, which is difficult to distinguish with TEM analysis. From this simple model calculation, it is concluded that the IrO_x particle size is influenced mainly by the precursor solution properties and the nozzle temperature. Further growth of IrO_x particles is not observed with current flame conditions.

It is worth pointing out that similar IrO_x particle size distributions with flame condition F1 and F2 suggests that further growth of IrO_x particles was not facilitated in the flame. Usually, higher precursor concentration creates more nucleus and monomers in the flame for nucleation growth [58,67]. Moreover, higher precursor flow rate and

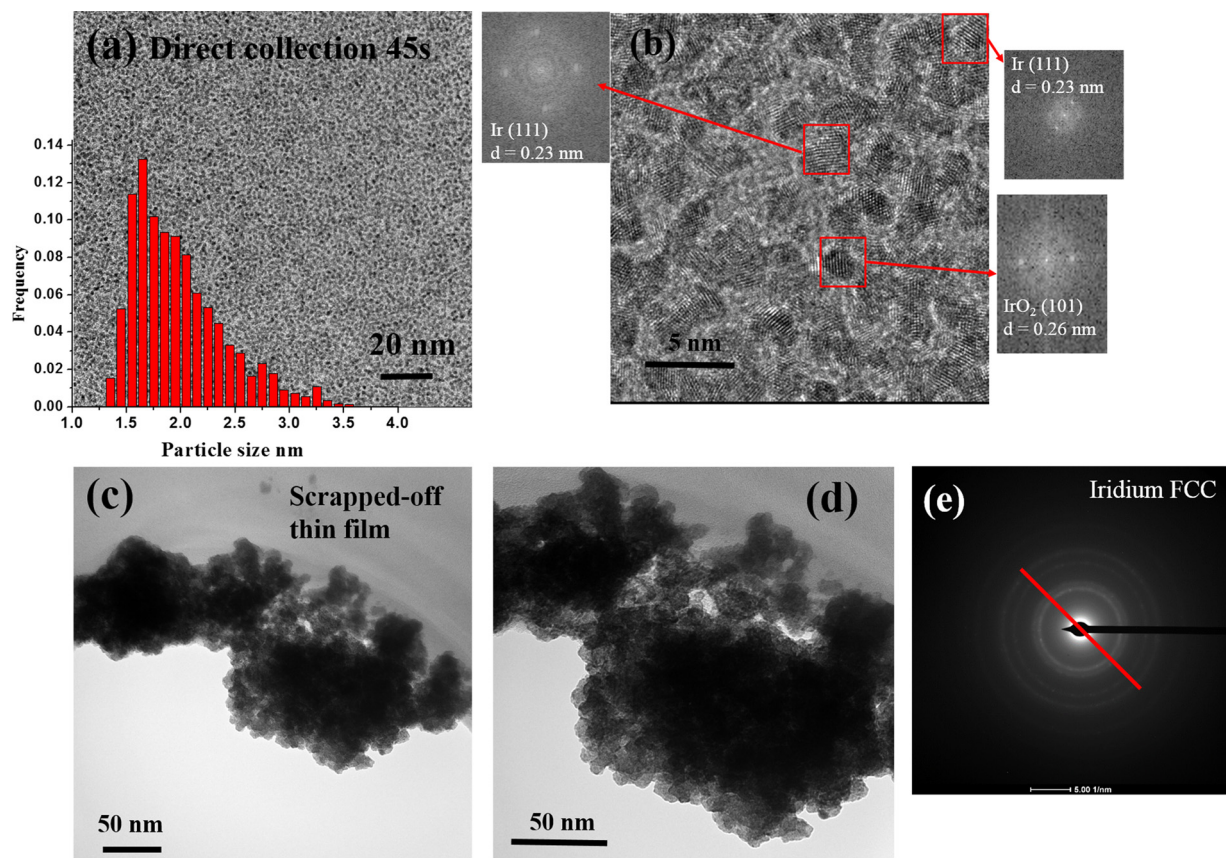


Fig. 2. (a, b) The bright field TEM images on IrOx particles deposited with F2 condition. The Nafion® slurry were not co-sprayed with the iridium precursor. A total of ~ 2900 particles were included to derive the particle size distribution histogram. FFT analysis of selected area in (b) are shown. (c, d) The IrOx/Nafion® agglomerates deposited with condition F2 and N2. (e) The electron diffraction pattern of (a) with a line to show where the intensity profile is determined to measure the d spacing.

Table 4

Analysis of electron diffraction patterns in Figs. 1e and 2e. Standard d spacing of iridium FCC structure are obtained from JCPDS 01-088-2342.

Planes	Measured d spacing in Fig. 1e (nm)	Measured d spacing in Fig. 2e (nm)	Standard d spacing (nm)
(111)	0.224736	0.226177	0.225167
(200)	0.194551	0.195332	0.195000
(220)	0.137129	0.139668	0.137886
(311)	0.117087	0.119189	0.117589

longer air quench distance provide longer high-temperature nucleation zone for particle growth [59,67]. The sinter-resistant behavior of iridium nanoparticles is predicted based on density functional theory (DFT) by Pawluk et al [68]. Watzky and Finke [69] found that energy barriers can prevent the growth of larger iridium nanoparticles and the stable iridium nanoparticles are formed where the energy is at a local minimum. A series of energy local minima is calculated by Watzky and Finke [69] which contains a certain number of atoms: 147, 309, 561, 923 (and so on), corresponding to particle size of 1.5 nm, 2.1 nm, 2.6 nm, 3.0 nm (and so on). The particle size distributions (Figs. 1 and 2) shows a majority of particles fall in the range of 1.5–2.1 nm and further particle growth is inhibited. It is likely that the current flame conditions provide insufficient heat to overcome the energy barrier.

The morphology of the IrOx/Nafion® catalyst layer deposited on Nafion® membrane are shown in Fig. 4 using various flame conditions (F1 or F2) and Nafion® solution spray conditions (N1 or N2). The cross-sectional images are displayed in Fig. 4a–c and the catalyst layer surfaces are displayed in Fig. 4e–g. The morphology of the IrOx/Nafion® catalyst layer shows that the IrOx/Nafion® agglomerates are packed on

the membrane. Having a low iridium precursor flow rate produces a thin layer where small IrOx/Nafion® agglomerates are packed to form larger spherical agglomerates, represented by the dashed circles in Fig. 4a. The catalyst layer thickness is 1.2–1.5 μm and the diameter of spherical agglomerates ranges between 1.2–2.1 μm (Fig. 4e). On the other hand, high iridium precursor flow rate produces a film with agglomerates packed to form layers parallel with the membrane surface (Fig. 4d). The formation of these horizontal layers can be attributed to the increase of the IrOx content in the anode when higher iridium precursor flow rate (F2) is coupled with lower Nafion® concentration in the slurry (N2). The surface morphology of the catalyst layer shows a drastic difference between the Nafion® solution spray conditions, N1 and N2. At higher Nafion® concentration and flow rate (N1), the surface is populated with spherical IrOx/Nafion® agglomerates. These agglomerates have a diameter of 1–3 μm at lower iridium precursor flow rate (Fig. 4a,e) and ~20 μm at a higher iridium precursor flow rate (Fig. 4f). Therefore, both the Nafion® solution flow rate and the Nafion® concentration need to be reduced to mitigate the inhomogeneity of the catalyst layer surface. The number of IrOx/Nafion® agglomerates is significantly reduced for cell-3 (Fig. 4g), albeit not eliminated.

3.2. Electrochemical measurement of OER

RDE test was performed to study the electrochemical behavior of IrOx/Nafion® catalyst synthesized using RSDT process. The iridium surface oxidation and reduction reactions are shown in the CV (Fig. 5a) where a comparison is made between F1 and F2 conditions. IrOx synthesized from both F1 and F2 conditions shows an absence of hydrogen adsorption/desorption. This suggests that the iridium particles in both samples are completely covered with iridium oxides on the surface

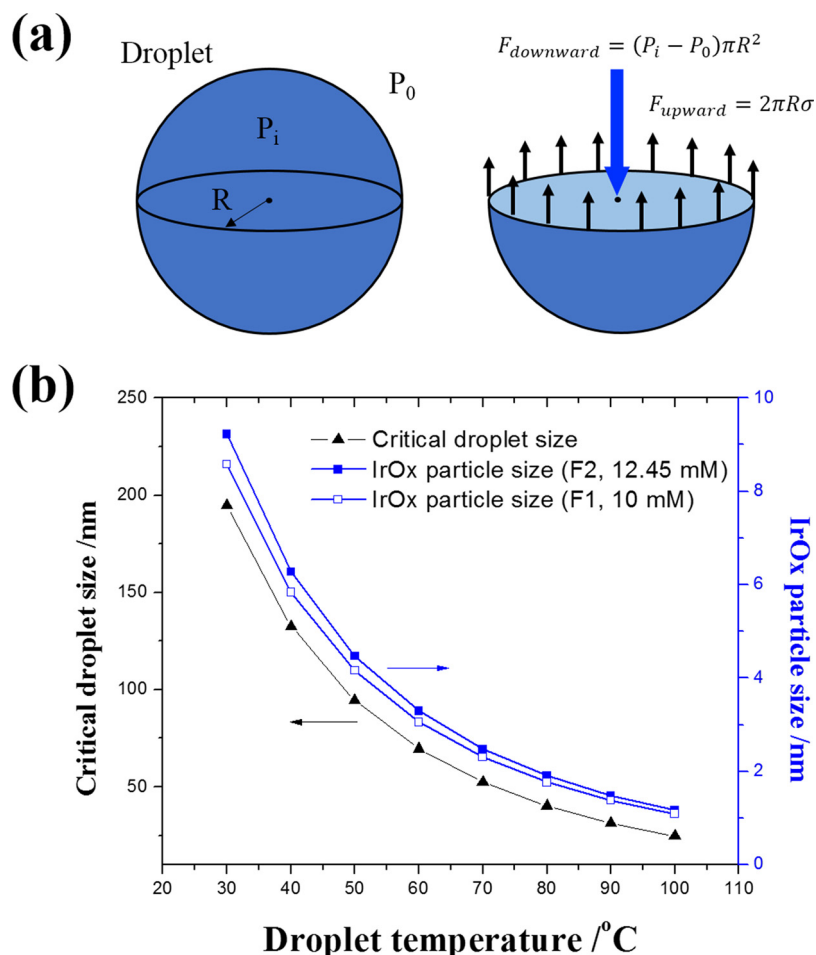


Fig. 3. (a) Force balance on a mid-cross section of a precursor droplet. (b) Critical droplet size and the resulting IrOx particle size as a function of droplet temperature at different flame conditions and precursor concentrations.

[56]. Limited hydrogen adsorption/desorption can still be observed for planar iridium disk electrode covered with a thick oxide layer [38]. This is because the anodically formed oxide layer is porous and thus metallic iridium sites are accessible to protons in the electrolyte [38]. On the other hand, the surface of nano-size iridium oxide particles is

oxidized in the RSDT process and therefore no hydrogen adsorption/desorption is shown in the CVs.

Both F1 and F2 samples exhibit three redox pairs in the CV, labeled as A1/C1, A2/C2 and A3/C3 following the nomenclature in [56]. The redox pairs of A1/C1 which occurs around 0.4 V (vs. RHE) are

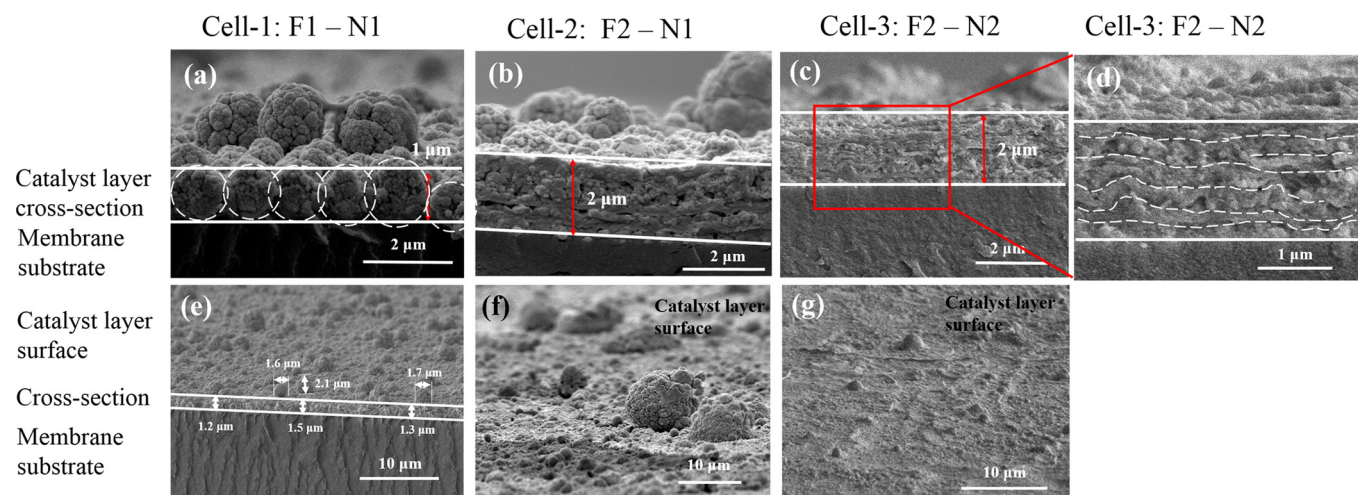


Fig. 4. Comparison of morphologies of RSDT-derived IrOx/Nafion® anodes deposited on Nafion® membrane. Flame and Nafion® spray conditions are listed on top of the images. (a-d) The cross-sectional morphology. (e-g) The electrode surface at a lower magnification. (d) Magnified region in (c) where horizontally layered structures can be seen. (a,e) F1 and N1 conditions, with deposition time of 180 min; (b, f) F2 and N1 conditions, with deposition time of 180 min; (c, g) F-2 and N-2 conditions, with deposition time of 55 min.

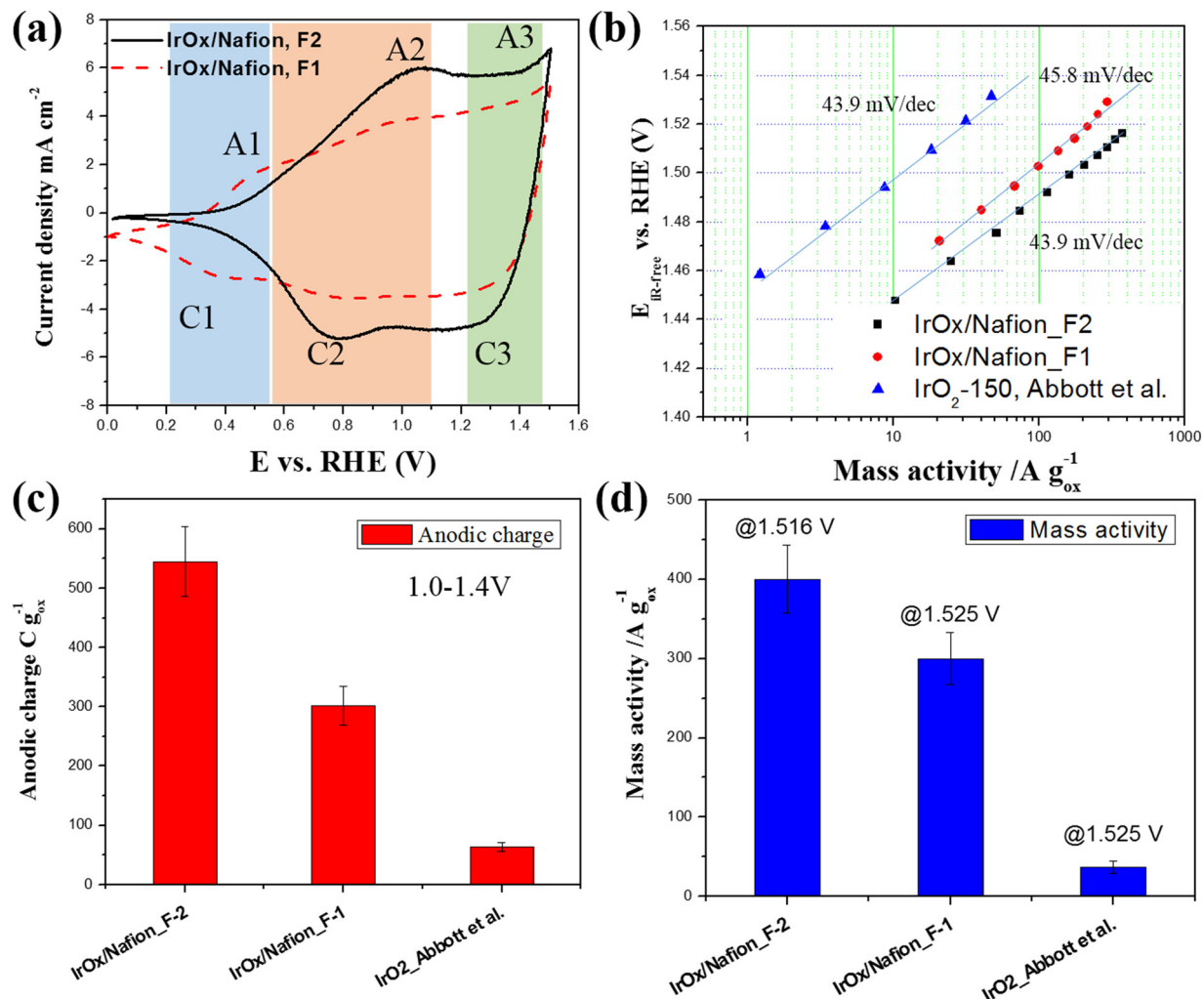


Fig. 5. (a) Cyclic voltammetry of IrOx/Nafion® catalyst synthesized using RSDT process with F1 and F2 conditions. (b) Quasi-stationary polarization curves for OER from 1.45 to 1.69 V (vs. RHE) with 20 mV step and 5 min dwell time at each potential. (c) Anodic charge integrated from the CV from 1.0 to 1.4 V (vs. RHE). (d) Comparison of OER mass activity and specific activity at 1.525 V (vs. RHE, iR-free). Note that the iR-free potential of F2 sample did not reach 1.525 V and the highest potential, 1.516 V, was used for mass activity comparison.

attributed to the formation of iridium (III) hydroxide [70]. The A1/C1 pair of F1 sample are much more pronounced than that of F2 sample, indicating that the F1 sample has more Ir(III) species on the surface than the F2 sample. On the contrary, the A2/C2 redox pairs are more pronounced in the F2 sample. The A2/C2 peak are due to the facile protonation and deprotonation of iridium (IV) hydroxide ($\text{IrO(OH)}_2 - \text{IrO}_2\text{H}_2\text{O}$) [29,38]. Thus, the F2 sample has more Ir (IV) species available on the surface than the F1 sample. Since the Ir(IV) species are the precursor for the binuclear mechanism of OER, the F2 sample exhibits higher anodic charge and OER activity than the F1 sample (Fig. 5b–d), although the iridium oxide particle size is similar between the two samples. Lastly, the A3/C3 redox pair located around 1.45 (vs. RHE) are related to the formation of Ir (V) species which serve as the precursor for oxygen evolution [38]. However, experimental evidence for Ir (V) species is lacking in the literature and debates remain regarding this redox pair as mentioned in the introduction section.

Comparing with IrOx nanoparticles that have a similar average particle size synthesized using Adam's fusion method [33], the RSDT-derived IrOx/Nafion® catalyst shows higher mass activity and anodic surface charge (Fig. 5b–d). Fig. 5b shows the quasi-stationary polarization curves plotted against the mass activity. The ohmic resistance was corrected with HFR measured with EIS. Since the purpose of EIS is only for ohmic resistance correction, the spectra are not presented in this work. The potential window before IR-correction is 1.49 V–1.69 V

(vs. RHE). Gas bubbles were observed to accumulate on the electrode surface at > 1.7 V (vs. RHE) and they could not be removed effectively by rotation. This could lead to unstable measurements of current due to extra mass transport limitations or ohmic resistance. The Tafel slopes are 43–46 mV/dec. for both RSDT-derived IrOx/Nafion® catalysts and the IrO_2 nanoparticles reported in [33], which agrees with the OER mechanism (Scheme 1b). The anodic charge and the mass activity for the RSDT-derived IrOx/Nafion® synthesized in F1 and F2 conditions are 5 times and 10 times higher, respectively, than the IrO_2 nanoparticles reported in [33], despite having similar average particle size. This can be attributed to the fact that RSDT-derived IrOx particles are well-dispersed in the Nafion® ionomer which offers higher catalyst utilization than for a ink-deposited RDE electrode. Additionally, since the anode catalyst layer is always flooded during RDE test, hydrated Nafion® ionomer provides water channels [71] that are accessible to the iridium particles. On the other hand, the electronic structure for RSDT-derived IrOx particles could be different from the IrOx particles synthesized from Adam's fusion method as the thermal history of the particles are different. The following session will exam the electronic structure of RSDT-derived IrOx particles in detail.

3.3. The electronic structure of iridium

The electrochemical behaviors (Fig. 5) can be corroborated with

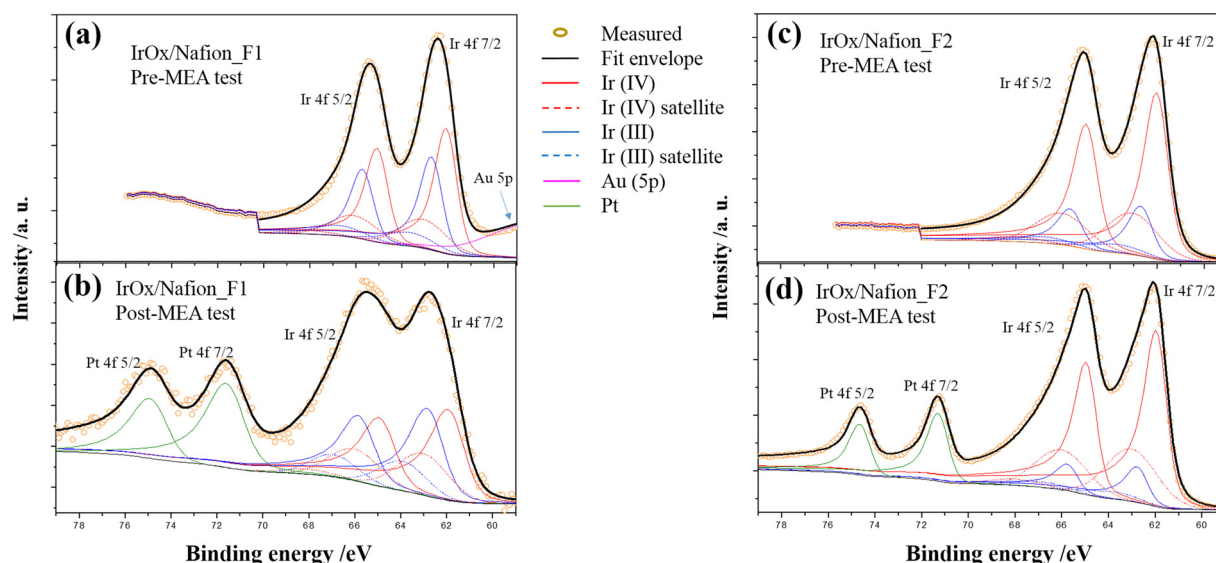


Fig. 6. (a) X-ray photoelectron spectra of Ir 4f for F1 (Cell-1) sample pre-MEA test. (b) X-ray photoelectron spectra of Ir 4f for F1 (Cell-1) sample post-MEA test. (c) X-ray photoelectron spectra of Ir 4f for F2 (Cell-5) sample pre-MEA test. (d) X-ray photoelectron spectra of Ir 4f for F2 (Cell-5) sample post-MEA test. The appearance of Au signal is because the specimen was sputter-coated with Au for SEM imaging. The appearance of Pt signal in the post-MEA test specimen is due to the contamination from the Pt plated Ti GDL.

Table 5

Compositions and positions of iridium species for the pre- and post-MEA test F1 and F2 samples.

Sample ID	Iridium species	Percentage, %	7/2 position, eV	5/2 position, eV	Line shape	FWHM, eV
F1 pre-test	Ir IV	59.34	62.06	65.06	DS (0.1, 100) SGL (45)	1.1
	Ir III	40.66	62.71	65.71	DS (0.1, 100) SGL (45)	1.1
F1 post-test	Ir IV	63.08	61.98	64.98	DS (0.15, 100) SGL (45)	1.63
	Ir III	36.92	62.96	65.96	DS (0.15, 100) SGL (45)	1.63
F2 pre-test	Ir IV	78.37	62.08	65.08	DS (0.1, 100) SGL (45)	1.16
	Ir III	21.64	62.74	65.74	DS (0.1, 100) SGL (45)	1.16
F2 post-test	Ir IV	84.33	62.03	65.03	DS (0.15, 100) SGL (45)	1.06
	Ir III	15.67	62.84	65.84	DS (0.15, 100) SGL (45)	1.06

XPS analysis of the surface oxides species. Due to the metallic character of iridium oxide [72], the fitting model proposed by Pfeifer et al [40] was employed in XPS analysis where an asymmetric Doniach-Sunjic (DS) line shape was used together with shake-up satellite peaks. The fitting parameters have been adjusted to fit the data considering the changes of X-ray sources and other instrumentation factors [73]. All spectra are corrected with the peak of adventitious carbon (C 1 s) following the method in [73]. The DS line shape fits well to the spectra of IrOx/Nafion® samples synthesized using F1 and F2 flame conditions (Fig. 6). The composition and binding energies of surface iridium species pre- and post-MEA tests are summarized in Table 5. Note that the iridium spectra cannot be fitted satisfactorily with either type of iridium species and both F1 and F2 samples show a co-existence of Ir (IV) and Ir (III) [39].

The spectra for the fresh IrOx/Nafion® samples are displayed in Fig. 6a and c. For the F1 sample, the measured peak positions for Ir 4f 7/2 and Ir 4f 5/2 are shifted slightly toward higher binding energy than the F2 sample. This is because the binding energy for Ir (III) is higher than that for Ir (IV) and the F1 sample has higher Ir (III) content than the F2 sample. Consequently, the ratio between Ir (IV) and Ir (III) is ~6:4 for the F1 sample, while a higher ratio, 8:2, is found for the F2 sample. The F2 condition has a longer high temperature zone which facilitates longer residence time for the iridium oxide nanoparticles to be calcined [59]. Thus, more Ir (IV) species is present with the F2 sample. A similar trend is found for the IrOx particles reported in [33] where higher calcination temperature produced particles with more Ir (IV) oxide. The results of XPS are in good agreement with the RDE measurement (Fig. 5) where the F2 sample shows a higher A2/C2 redox measurement (Fig. 5) where the F2 sample shows a higher A2/C2 redox

couple which are attributed to the facile protonation and deprotonation of iridium (IV) hydroxide. Since the Ir (IV) serves as the precursor for the binuclear OER mechanism, the higher Ir (IV) on the surface facilitates higher OER activity.

The post-test Ir 4f spectra are shown in Fig. 6b and d. For both F1 and F2 samples, the composition of Ir (IV) increased by a few percent but do not deviate far from the ratio before the MEA test (Table 5). The Ir (III) content remains high in the post-MEA F1 sample. The F1 sample was able to run for only 22 h (Cell 1). The low stability of F1 sample can be attributed to the higher Ir (III) content which undergoes direct dissolution in the oxygen evolution circle (Scheme 1). In contrast, the F2 sample can maintain a high content of Ir (IV) after the stability test. The duration of stability test for the F2 sample (Cell-5) is ~4,500 h, significantly longer than the F1 sample (Cell-1). Thus, it is crucial to maintain a high content of Ir (IV) at both pre- and post-test anode surfaces to achieve high stability.

The oxygen 1 s spectra of pre- and post-MEA tests are shown in Fig. 7. The results of surface oxygen species compositions and binding energies are summarized in Table 6. Deconvolution of the spectra shows three oxygen species which can be attributed to metal oxide, hydroxide and the contribution from water and adventitious carbon [33,74]. An asymmetric line shape is used for the metal oxide peak due to the screening effect from conduction electrons in iridium oxide [74]. From Table 6 the content of hydroxide is higher for the F1 sample, which agrees with the result from Table 5 where the F1 sample has a higher Ir (III) content. Furthermore, the fresh samples show an oxide to hydroxide (O: OH) ratios of 0.21 and 0.37 respectively, for F1 and F2 samples. If Ir(IV) were present only in the IrO_2 phase, the O:OH ratio

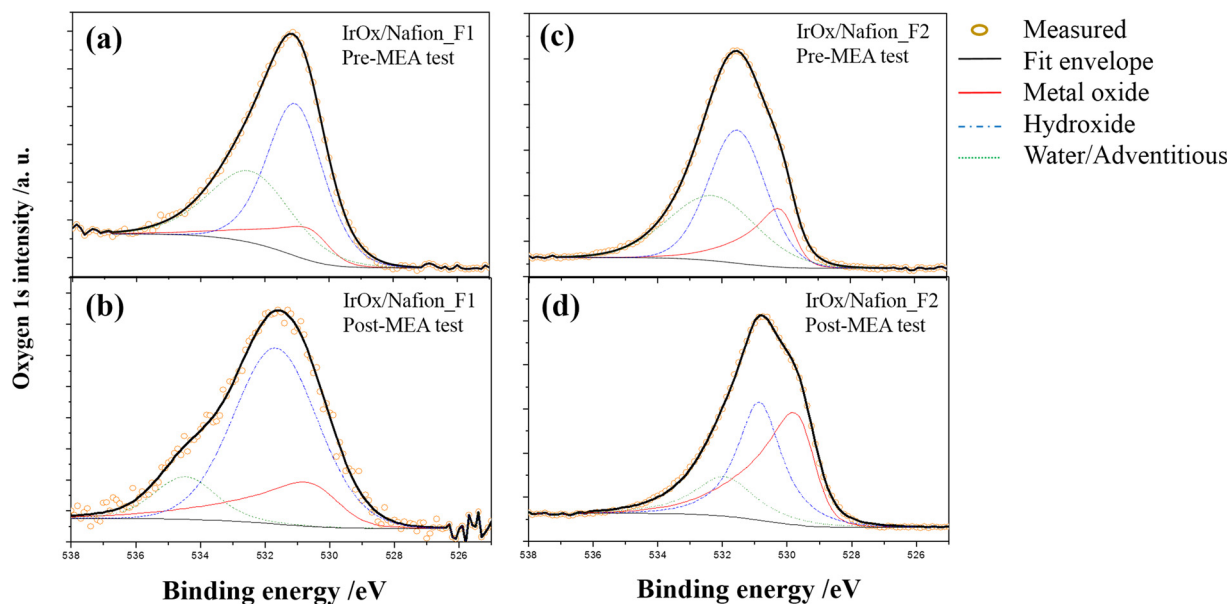


Fig. 7. (a) X-ray photoelectron spectra of O 1s for F1 (Cell-1) sample pre-MEA test. (b) X-ray photoelectron spectra of O 1s for F1 (Cell-1) sample post-MEA test. (c) X-ray photoelectron spectra of O 1s for F2 (Cell-5) sample pre-MEA test. (d) X-ray photoelectron spectra of O 1s for F2 (Cell-5) sample post-MEA test.

should be at higher values of 1 and 2.6, respectively, for F1 and F2 samples. This suggests that the hydroxide not only contains Ir(III)(OH)₃ but also Ir(IV) hydroxide. The presence of both Ir(III) and Ir(IV) hydroxide imply that the atomic ratio between oxygen and iridium is close to 3. Indeed, the pre-test samples shows that the atomic ratio of O/Ir is about 2.9 ± 0.2 , evidence for the high content of hydroxide on the surface. Additionally, high content of hydroxide (low O:OH ratio) is beneficial for OER activity [31,32,35]. The O: OH ratio of RSDT-derived IrO_x samples are 0.21 and 0.37 for F1 and F2 samples, respectively. These ratios are lower than the IrO_x particles synthesized using Adam's fusion method [33] which is 0.51. Thus, higher OER activity was measured for the RSDT-derived IrO_x particles (Fig. 5b-d). The post-test spectra of both F1 and F2 samples show an increase of the metal oxide content. In particular, the O: OH ratio of the F2 samples increased significantly from 0.37 to 1.1, whereas O:OH ratio of the F1 samples increased only slightly from 0.21 to 0.30. The F2 sample was tested for a much longer operating time than the F1 sample and thus, more hydroxide was oxidized during OER. Furthermore, the F2 sample has high Ir (IV) content at both pre and post-MEA test. More Ir is available for further oxidation to oxide and thus, the O: OH ratio increased significantly after MEA test. On the other hand, the F1 sample maintained a high Ir (III) content even after MEA test which can contribute to a higher hydroxide content, or lower O: OH ratio.

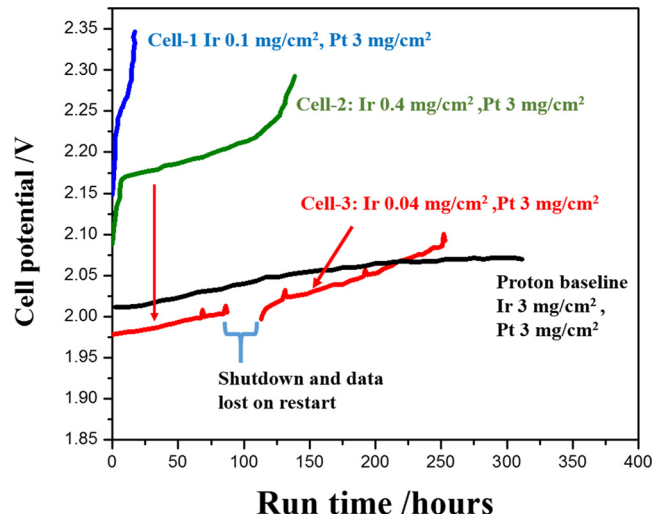


Fig. 8. Comparison of electrolysis operation for RSDT anodes (Cell-1,2,3) with morphology and process conditions shown in Fig. 4 and Table 3. Test performed using circular 28 cm² cell at 80 °C with 1.8 A m⁻² current load and 2.76 MPa (400 psi) hydrogen pressure. The cathode for the RSDT cells are commercial Pt black GDE with 3 mg cm⁻² Pt loading provided by Proton OnSite.

Table 6

Compositions and positions of oxygen species for the pre- and post-MEA test F1 and F2 samples [29,33,74].

Sample ID	Oxygen species	Percentage, %	Position, eV	Line shape	FWHM, eV
F1 pre-test	Metal oxide	12.63	530.45	LF (0.3, 1.5, 25, 150)	1.58
	Hydroxide	51.98	531.1	GL (30)	2.08
	Adventitious, water	35.39	532.5	GL (30)	3.03
F1 post-test	Metal oxide	15.78	530.4	LF (0.3, 1.5, 25, 150)	2.3
	Hydroxide	54.4	531.67	GL (30)	3
	Adventitious, water	29.82	534.44	GL (30)	2.3
F2 pre-test	Metal oxide	17.64	530.1	LF (0.3, 1.5, 25, 150)	1.15
	Hydroxide	47.05	531.5	GL (30)	2.1
	Adventitious, water	35.31	532.3	GL (30)	3.2
F2 post-test	Metal oxide	43.88	530.06	LF (0.3, 1.5, 25, 150)	1.45
	Hydroxide	38.47	531.35	GL (30)	1.62
	Adventitious, water	17.65	532.43	GL (30)	2.21

3.4. Long-term PEM electrolysis performance

The electrolysis performance of Cell-1, 2 and 3 are shown in Fig. 8 where the effect of processing conditions and anode catalyst layer morphology is investigated. The anode stability is improved from ~22 h (Cell-1) to ~120 h (Cell-2) as the flame condition is changed from F-1 to F-2. The anode stability is further improved to 250 h (Cell-3) accompanied with a cell performance improvement of ~200 mV when the Nafion® solution spray condition changes from N1 to N2. This suggests that reducing the surface agglomerates of the anode catalyst layer plays a vital role in the anode performance. Under high compression, the surface agglomerates are likely to collapse and disrupt the anode catalyst layer, leading to inhomogeneous current distribution, cell compression and a partially blocked Ti GDL. In addition, while the deposition time of Cell-3 was a third of Cell-2 (Table 3), the iridium loading was only 1/10. Yet, both samples show a catalyst layer thickness of ~2 μm (Fig. 4). This implies that the large surface IrO_x/Nafion® agglomerates used up to ~90% of the iridium loading in Cell-2 and that the reduction of these agglomerates improves the utilization of iridium.

Based on the results in Fig. 8, CCMs (Cell-4 and 5) were fully fabricated using RSDT process with the same anode conditions as Cell-3 and the cathode conditions as in ref. [60] for both cells. For the anode, Cell-5 has double iridium loading on the anode than that of Cell-4. The long-term electrolysis test (Fig. 9) shows that increasing iridium loading significantly improved the anode stability and reduced the cell potential at beginning-of-test (BOT). Cell-5 achieved an outstanding ~4,500 h of operation with scaled-up 86 cm² active area. The cell potential shows two degradation rates throughout the test period. For the first 2,500 h, the degradation rate is 36.5 μV h⁻¹, followed by a shutdown at 2500 h and recovery period till 3,500 h. Further operation up to 4543 h saw a reduced rate of 11.5 μV h⁻¹. The baseline cell shows a degradation rate of 11 μV h⁻¹ for 2,000–6,000 h of operation. Comparing with the baseline performance, the RSDT Cell-5 reached similar degradation rate beyond 3750 h of operation with 1/30th the iridium loading on the anode and 1/10th the platinum loading on the cathode. Note that the discontinuity occurred at ~2,500 h is due to a complete cell shutdown for ~3 days. The cell performance was recovered after restart. This phenomenon was also seen for Cell-4 and the baseline. The recovery of cell performance is attributed to the partial reduction of the surface oxidation of the Ti GDL. [20]

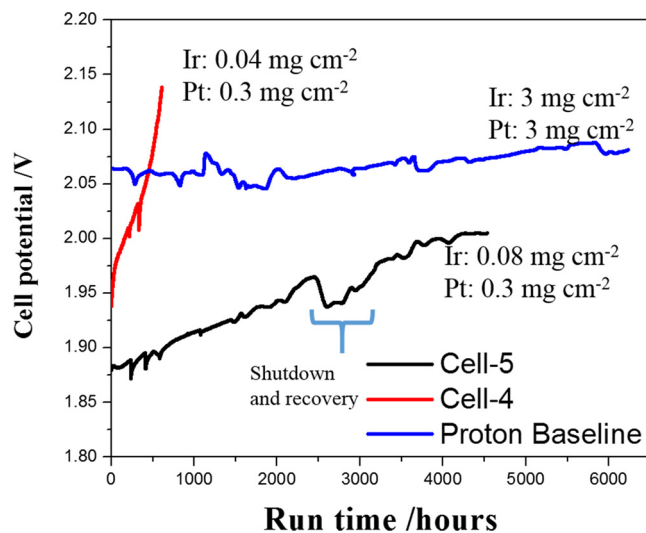


Fig. 9. Long-term electrolysis operation of CCM fully fabricated by RSDT process: Cell-4 and Cell-5 (specifications can be found in Table 3). Test performed at 80 °C with 1.8 A cm⁻² current load and 2.76 MPa (400 psi) hydrogen pressure. The baseline is acquired from Proton OnSite's commercial cell with 86 cm² active area and operated at 50 °C with 1.8 A cm⁻² current load and 2.76 MPa (400 psi) hydrogen pressure.

Table 7
Degradation rates reported in the literature for iridium-based catalysts.

References	Anode catalyst	Ir loading, mg cm ⁻²	Cathode catalyst	Pt loading, mg cm ⁻²	Operating current, A cm ⁻²	Operating temperature, °C	Electrode fabrication process	Active area	Test period, hours	Degradation rate, μV h ⁻¹
Grigoriev et al. [24]	Ir black	1.5	Pt/Vulcan XC-72	0.5	60	spraying	25	4000	35.5	
Rozain et al. [23]	IrO ₂ /Ti	0.12	Pt/C, TKK	0.25	1	80	spraying	25	1000	27
Rozain et al. [23]	IrO ₂	0.32/0.1	Pt/C, TKK	0.25	1	80	spraying	5	1000	110/180 ^a
Siracusano et al. [22]	IrO ₂	0.4	Pt/Vulcan XC-72	0.1	1.0	80	spray-coating	5	1000	12
Rakousky et al. [21]	IrO ₂ and TiO ₂	2.25	Pt/C	0.8	2.0	80	Commercial	17.64	1150	1.94
Lettenmeier et al. [20]	Ir black	1	Pt black	0.9	2.0	55–60	Commercial	120	400	Not significant
Lewinski et al. [17]	Ir-NSTF	0.25	Pt-NSTF	0.25	2	80	3M	50	5000	Average 6.8
RSDT Cell-5	IrO _x and Nafion®	0.08	Pt/Vulcan XC-72R	0.3	1.8	80	RSDT	86	4543	36.5, 11.5
Wang et al. [19]	Ir _{0.7} Ru _{0.3} O _x	1 ^b	Pt/C	0.4	1	80	Air-brush spraying	25	400	Not significant
Siracusano et al. [18]	Ir _{0.7} Ru _{0.3} O _x	0.34 ^b	Pt/Vulcan XC-72	0.1	1.0/3.0	80	spray-coating	5	1000	15/23 ^c

^a Degradation rate at 0.32 and 0.1 mg cm⁻² Ir loading, respectively.

^b Loading of Ir and Ru combined.

^c Degradation rate at 1.0 and 3.0 A cm⁻², respectively.

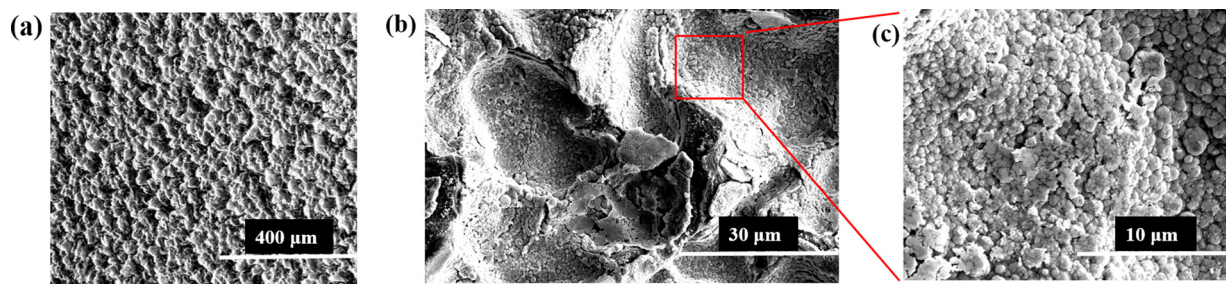


Fig. 10. Anode surface morphology of post-stability test (Cell-5).

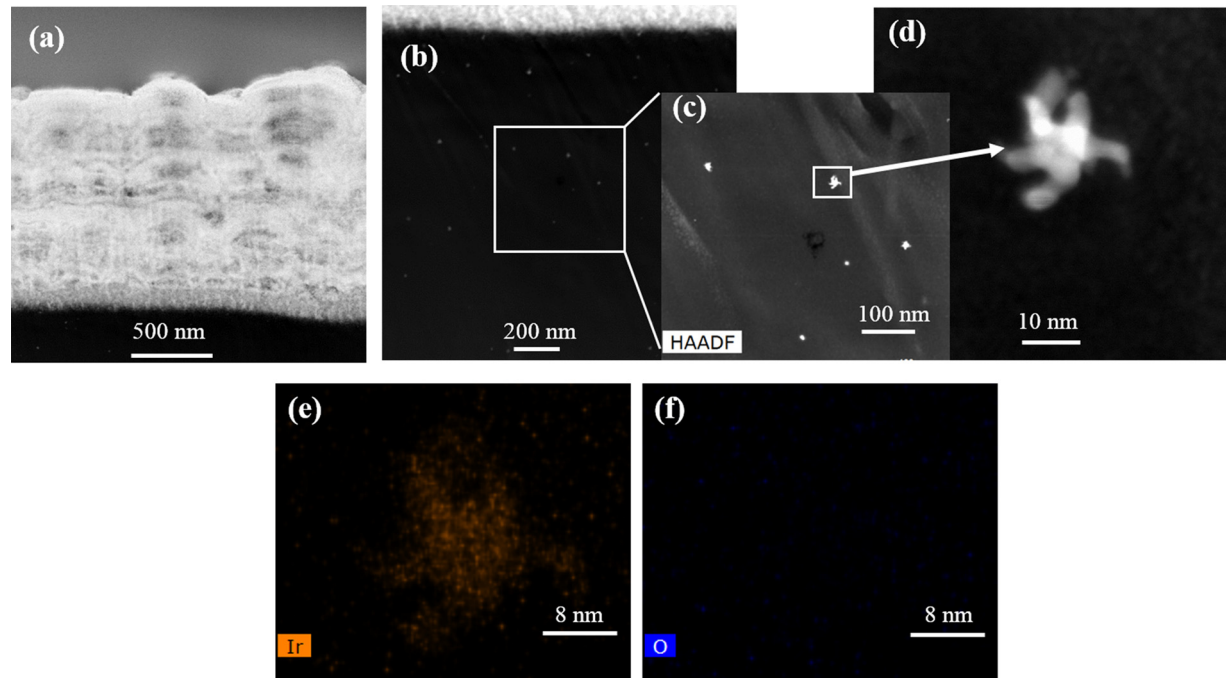


Fig. 11. (a) Cross-sectional HAADF image of the anode catalyst layer. (b) Cross-sectional HAADF image of the membrane region adjacent to the anode catalyst layer. (c, d) Enlarged area of the membrane region showing the presence of iridium deposits. (e, f) Chemical mapping of iridium and oxygen for the iridium deposit in (d).

Recent studies on long-term electrolysis tests of iridium-based catalysts have shown various operating times and degradation rates (Table 7). The degradation rate of pure iridium or iridium oxide at low current density operation ($0.5\text{--}1\text{ A cm}^{-2}$) is generally less than $100\text{ }\mu\text{V h}^{-1}$. [22,24] But degradation rates increase to $> 100\text{ }\mu\text{V h}^{-1}$ as the anode iridium loading decreases to less than 1 mg cm^{-2} . [23] Incorporation of catalyst support (Ti) shows significant reduction of degradation [23], but not applicable to high current density operation (2 A cm^{-2}) where the degradation rate is increased to $\sim 200\text{ }\mu\text{V h}^{-1}$. [21] Of all the studies listed in Table 7, NSTF catalyst shows the lowest average degradation rate of $6.8\text{ }\mu\text{V h}^{-1}$, with low noble metal loading ($0.5\text{ mg}_{\text{Pt+Ir}}\text{ cm}^{-2}$) and at 2 A cm^{-2} current density. [17] The RSDT Cell-5 is competitive as it not only demonstrated the stability approaching $5,000\text{ h}$, but also used the lowest noble metal loading ($0.4\text{ mg}_{\text{Pt+Ir}}\text{ cm}^{-2}$). Furthermore, comparing with NSTF catalyst fabricated using vacuum sputtering method, RSDT is a cost-effective process that fabricates CCMs in an open atmosphere and combines catalyst synthesis and electrode fabrication into one step. Additionally, iridium/ruthenium mixed oxide, which has also been deposited by RSDT [75], has emerged as a promising anode catalyst [18,19]. However, longer operation time is needed in order to verify the catalyst stability.

3.5. Degradation of IrO_x/Nafion® catalyst

Post-test analysis of Cell-5 CCM are shown in Figs. 10 and 11. The

surface morphology post-test anode (Fig. 10) shows indented surface due to compression from the anode GDL (porous Ti plate). A similar observation has also been reported in [7]. The cross-section TEM analysis (Fig. 11) was carried out using FIB lift-out technique. The specimen was taken at the center of the imprint, an area like Fig. 10c. Fig. 11a shows an anode catalyst layer thickness about $1.7\text{ }\mu\text{m}$ which is thinner than the as-deposited $2\text{ }\mu\text{m}$ anode thickness (Fig. 4c). This indicates that the anode catalyst layer has been compressed during MEA assembly and/or after long-term operation. Examination of the membrane region adjacent to the anode catalyst layer (Fig. 11b) reveals iridium deposits which are likely formed due to iridium dissolution and re-deposition in the membrane. XEDS analysis of one of the iridium deposits (Fig. 11d) shows that it is mostly metallic iridium (Fig. 11e, f), confirming the re-deposition process of iridium ions migrated towards the membrane.

4. Conclusions

In this study we report a nano-size IrO_x/Nafion® composite catalyst that exhibits outstanding activity for oxygen evolution reaction (OER) and stability in a PEM water electrolyzer. The capability of full electrolyzer cell fabrication with the RSDT process is demonstrated and the RSDT cell achieved $\sim 4,500\text{ h}$ of stable electrolysis operation at 1.8 A cm^{-2} and 80°C with ultra-low iridium loading of 0.08 mg cm^{-2} on the anode and platinum loading of 0.3 mg cm^{-2} on the cathode.

Furthermore, the IrO_x/Nafion® catalyst shows 10 times the OER mass activity compared to that of IrO_x nanoparticles prepared from wet chemistry method. Combining the results from electrochemical measurements and XPS revealed that the surface of RSDT-derived IrO_x catalyst is mostly iridium hydroxide with a mixed valence of Ir (III) and Ir (IV) species. To achieve both high OER activity and stability, three key factors have been identified: (1) high ratio of Ir (IV) to Ir (III) species and high content of hydroxide on the surface; (2) high anodic charge and surface area due to nano-size IrO_x particles well-dispersed in the Nafion® ionomer electrolyte; (3) homogeneous anode catalyst layer morphology. The post-test CCM shows an indented surface due to compression from the anode GDL. Iridium deposits formed due to iridium dissolution and re-deposition are identified in the membrane region adjacent to the anode catalyst layer. Further analysis on the post-test RSDT CCM will be carried out to develop a better understanding of the degradation mechanisms on both anode and cathode.

Acknowledgements

This work is funded by DOE SBIR contract DE-FOA-0000957. The authors would like to thank Dr. Timothy Myles' initial work on the model of particle formation in RSDT process.

References

- [1] A. Buttler, H. Spliethoff, Current status of water electrolysis for energy storage, grid balancing and sector coupling via power-to-gas and power-to-liquids: a review, *Renew. Sustain. Energy Rev.* 82 (2018) 2440–2454.
- [2] K.T. Møller, T.R. Jensen, E. Akiba, H. Li, Hydrogen - a sustainable energy carrier, *Prog. Nat. Sci.* 27 (2017) 34–40.
- [3] M. Götz, J. Lefebvre, F. Mörs, A. McDaniel Koch, F. Graf, S. Bajohr, et al., Renewable power-to-gas: a technological and economic review, *Renew. Energy* 85 (2016) 1371–1390.
- [4] S.E. Hosseini, M.A. Wahid, Hydrogen production from renewable and sustainable energy resources: promising green energy carrier for clean development, *Renew. Sustain. Energy Rev.* 57 (2016) 850–866.
- [5] S. Sharma, S.K. Ghoshal, Hydrogen the future transportation fuel: from production to applications, *Renew. Sustain. Energy Rev.* 43 (2015) 1151–1158.
- [6] A.S. Arico, S. Siracusano, N. Briguglio, V. Baglio, A. Di Blasi, V. Antonucci, Polymer electrolyte membrane water electrolysis: status of technologies and potential applications in combination with renewable power sources, *J. Appl. Electrochem.* 43 (2013) 107–118.
- [7] U. Babic, M. Suermann, F.N. Büchi, L. Gubler, T.J. Schmidt, Critical review—identifying critical gaps for polymer electrolyte water electrolysis development, *J. Electrochem. Soc.* 164 (2017) F387–F399.
- [8] A. Marshall, B. Børresen, H. Hagen, M. Tryspkin, R. Tunold, Hydrogen production by advanced proton exchange membrane (PEM) water electrolyzers—reduced energy consumption by improved electrocatalysis, *Energy* 32 (2007) 431–436.
- [9] P. Millet, R. Ngameni, S.A. Grigoriev, N. Mbemba, F. Brisset, A. Ranjbari, et al., PEM water electrolyzers: from electrocatalysis to stack development, *Int. J. Hydrogen Energy* 35 (2010) 5043–5052.
- [10] P. Millet, M. Mbemba, S.A. Grigoriev, V.N. Fateev, A. Aukaualo, C. Etievant, Electrochemical performances of PEM water electrolysis cells and perspectives, *Int. J. Hydrogen Energy* 36 (2011) 4134–4142.
- [11] M. Carmo, D.L. Fritz, J. Mergel, D. Stolten, A comprehensive review on PEM water electrolysis, *Int. J. Hydrogen Energy* 38 (2013) 4901–4934.
- [12] E. Fabbri, A. Habereder, K. Waltar, R. Kotz, T.J. Schmidt, Developments and perspectives of oxide-based catalysts for the oxygen evolution reaction, *Catal. Sci. Technol.* 4 (2014) 3800–3821.
- [13] T. Reier, H.N. Nong, D. Teschner, R. Schlogl, P. Strasser, Electrocatalytic oxygen evolution reaction in acidic environments: reaction mechanisms and catalysts, *Adv. Energy Mater.* 7 (2017) 1601275.
- [14] K.E. Ayers, E.B. Anderson, C. Capuano, B. Carter, L. Dalton, G. Hanlon, et al., Research advances towards low cost, high efficiency PEM electrolysis, *ECS Trans.* 33 (2010) 3–15.
- [15] N. Danilovic, K.E. Ayers, C. Capuano, J.N. Renner, L. Wiles, M. Pertoso, (Plenary) challenges in going from laboratory to megawatt scale PEM electrolysis, *ECS Trans.* 75 (2016) 395–402.
- [16] C. Spori, J.T.H. Kwan, A. Bonakdarpour, D.P. Wilkinson, P. Strasser, The stability challenges of oxygen evolving catalysts: towards a common fundamental understanding and mitigation of catalyst degradation, *Angew. Chem. Int. Ed.* 56 (2017) 5994–6021.
- [17] K.A. Lewinski, d.V. van, S.M. Luopa, NSTF advances for PEM electrolysis - the effect of alloying on activity of NSTF electrolyzer catalysts and performance of NSTF based PEM electrolyzers, *ECS Trans.* 69 (2015) 893–917.
- [18] S. Siracusano, N. Hodnik, P. Jovanovic, F. Ruiz-Zepeda, M. Šala, V. Baglio, et al., New insights into the stability of a high performance nanostructured catalyst for sustainable water electrolysis, *Nano Energy* 40 (2017) 618–632.
- [19] L. Wang, V.A. Saveleva, S. Zafeiratos, E.R. Savinova, P. Lettenmeier, P. Gazdzicki, et al., Highly active anode electrocatalysts derived from electrochemical leaching of Ru from metallic Ir_{0.7}Ru_{0.3} for proton exchange membrane electrolyzers, *Nano Energy* 34 (2017) 385–391.
- [20] P. Lettenmeier, R. Wang, R. Abuatallah, S. Helmly, T. Morawietz, R. Hiesgen, et al., Durable membrane electrode assemblies for proton exchange membrane electrolyzer systems operating at high current densities, *Electrochim. Acta* 210 (2016) 502–511.
- [21] C. Rakousky, U. Reimer, K. Wippermann, M. Carmo, W. Lueke, D. Stolten, An analysis of degradation phenomena in polymer electrolyte membrane water electrolysis, *J. Power Sources* 326 (2016) 120–128.
- [22] S. Siracusano, V. Baglio, S.A. Grigoriev, L. Merlo, V.N. Fateev, A.S. Aricò, The influence of iridium chemical oxidation state on the performance and durability of oxygen evolution catalysts in PEM electrolysis, *J. Power Sources* 366 (2017) 105–114.
- [23] C. Rozain, E. Mayousse, N. Guillet, P. Millet, Influence of iridium oxide loadings on the performance of PEM water electrolysis cells: part II-advanced oxygen electrodes, *Appl. Catal. B* 182 (2016) 123–131.
- [24] S.A. Grigoriev, D.G. Bessarabov, V.N. Fateev, Degradation mechanisms of MEA characteristics during water electrolysis in solid polymer electrolyte cells, *Russ. J. Electrochim.* 53 (2017) 318–323.
- [25] G. Liu, J. Xu, Y. Wang, X. Wang, An oxygen evolution catalyst on an antimony doped tin oxide nanowire structured support for proton exchange membrane liquid water electrolysis, *J. Mater. Chem. A Mater. Energy Sustain.* 3 (2015) 20791–20800.
- [26] J.O. Bockris, Kinetics of activation controlled consecutive electrochemical reactions: anodic evolution of oxygen, *J. Chem. Phys.* 24 (1956) 817–827.
- [27] S. Pierro, A. Kapalka, C. Comminellis, Electrochemical comparison between IrO₂ prepared by thermal treatment of iridium metal and IrO₂ prepared by thermal decomposition of H₂IrCl₆ solution, *Electrochim. Commun.* 12 (2010) 172–174.
- [28] S. Pierro, T. Nagel, H. Baltruschat, C. Comminellis, Investigation of the oxygen evolution reaction on Ti/IrO₂ electrodes using isotope labelling and on-line mass spectrometry, *Electrochim. Commun.* 9 (2007) 1969–1974.
- [29] R. Kötz, H. Neff, S. Stucki, Anodic iridium oxide films: XPS-studies of oxidation state changes and O₂-evolution, *J. Electrochim. Soc.* 131 (1984) 72–77.
- [30] A. Minguzzi, O. Lugaresi, E. Achilli, C. Locatelli, A. Vertova, P. Ghigna, et al., Observing the oxidation state turnover in heterogeneous iridium-based water oxidation catalysts, *Chem. Sci.* 5 (2014) 3591–3597.
- [31] V. Pfeifer, T.E. Jones, S. Wrabetz, C. Massue, J.J. Velasco Velez, R. Arrigo, et al., Reactive oxygen species in iridium-based OER catalysts, *Chem. Sci.* 7 (2016) 6791–6795.
- [32] V. Pfeifer, T.E. Jones, J.J. Velasco Velez, R. Arrigo, S. Piccinin, M. Havecker, et al., In situ observation of reactive oxygen species forming on oxygen-evolving iridium surfaces, *Chem. Sci.* 8 (2017) 2143–2149.
- [33] D.F. Abbott, D. Lebedev, K. Waltar, M. Povia, M. Nachtegaal, E. Fabbri, et al., Iridium oxide for the oxygen evolution reaction: correlation between particle size, morphology, and the surface hydroxo layer from operando XAS, *Chem. Mater.* 28 (2016) 6591–6604.
- [34] S. Geiger, O. Kasian, B.R. Shrestha, A.M. Mingers, K.J.J. Mayrhofer, S. Cherevko, Activity and stability of electrochemically and thermally treated iridium for the oxygen evolution reaction, *J. Electrochim. Soc.* 163 (2016) F3132–F3138.
- [35] C. Massue, V. Pfeifer, M. van Gastel, J. Noack, G. Algara-Siller, S. Cap, et al., Reactive electrophilic O⁺ species evidenced in high-performance iridium oxohydroxide water oxidation electrocatalysts, *ChemSusChem* 10 (2017) 4786–4798.
- [36] V. Pfeifer, T.E. Jones, J.J. Velasco Velez, C. Massue, M.T. Greiner, R. Arrigo, et al., The electronic structure of iridium oxide electrodes active in water splitting, *Phys. Chem. Chem. Phys.* 18 (2016) 2292–2296.
- [37] V.A. Saveleva, L. Wang, D. Teschner, T. Jones, A.S. Gago, K.A. Friedrich, et al., Operando evidence for a universal oxygen evolution mechanism on thermal and electrochemical iridium oxides, *J. Phys. Chem. Lett.* 9 (2018) 3154–3160.
- [38] S. Cherevko, S. Geiger, O. Kasian, A. Mingers, K.J.J. Mayrhofer, Oxygen evolution activity and stability of iridium in acidic media. Part 2. – electrochemically grown hydrous iridium oxide, *J. Electroanal. Chem.* 774 (2016) 102–110.
- [39] A. Minguzzi, C. Locatelli, O. Lugaresi, E. Achilli, G. Cappelletti, M. Scavini, et al., Easy accommodation of different oxidation states in iridium oxide nanoparticles with different hydration degree as water oxidation electrocatalysts, *ACS Catal.* 5 (2015) 5104–5115.
- [40] V. Pfeifer, T.E. Jones, J.J. Velasco Velez, C. Massue, R. Arrigo, D. Teschner, et al., The electronic structure of iridium and its oxides, *Surf. Interface Anal.* 48 (2016) 261–273.
- [41] J. Rossmeisl, A. Logadottir, J.K. Nørskov, Electrolysis of water on (oxidized) metal surfaces, *Chem. Phys.* 319 (2005) 178–184.
- [42] J. Rossmeisl, Z. Qu, H. Zhu, G. Kroes, J.K. Nørskov, Electrolysis of water on oxide surfaces, *J. Electroanal. Chem.* 607 (2007) 83–89.
- [43] A.H. Reksten, H. Thuv, F. Seland, S. Sunde, The oxygen evolution reaction mechanism at Ir_xRu_{1-x}O₂ powders produced by hydrolysis synthesis, *J. Electroanal. Chem.* 819 (2018) 547–561.
- [44] Z. Ma, Y. Zhang, S. Liu, W. Xu, L. Wu, Y. Hsieh, et al., Reaction mechanism for oxygen evolution on RuO₂, IrO₂, and RuO₂@IrO₂ core-shell nanocatalysts, *J. Electroanal. Chem.* 819 (2018) 296–305.
- [45] I.C. Man, H. Su, F. Calle-Vallejo, H.A. Hansen, J.I. Martínez, N.G. Inoglu, et al., Universality in oxygen evolution electrocatalysis on oxide surfaces, *ChemCatChem* 3 (2011) 1159–1165.
- [46] T. Nakagawa, C.A. Beasley, R.W. Murray, Efficient electro-oxidation of water near its reversible potential by a mesoporous IrO_x nanoparticle film, *J. Phys. Chem. C* 113 (2009) 12958–12961.

- [47] M.E.G. Lyons, S. Floquet, Mechanism of oxygen reactions at porous oxide electrodes. Part 2-oxygen evolution at RuO₂, IrO₂ and Ir_xRu_{1-x}O₂ electrodes in aqueous acid and alkaline solution, *Phys. Chem. Chem. Phys.* 13 (2011) 5314–5335.
- [48] H.G. Sanchez Casalongue, M.L. Ng, K. Sarp, F. Daniel, O. Hirohito, N. Anders, In situ observation of surface species on iridium oxide nanoparticles during the oxygen evolution reaction, *Angew. Chem. Int. Ed.* 53 (2014) 7169–7172.
- [49] N. Danilovic, R. Subbaraman, K.C. Chang, S.H. Chang, Y. Kang, J. Snyder, et al., Using surface segregation to design stable Ru-Ir oxides for the oxygen evolution reaction in acidic environments, *Angew. Chem. Int. Ed.* 53 (2014) 14016–14021.
- [50] N. Danilovic, R. Subbaraman, K. Chang, S.H. Chang, Y.J. Kang, J. Snyder, et al., Activity-stability trends for the oxygen evolution reaction on monometallic oxides in acidic environments, *J. Phys. Chem. Lett.* 5 (2014) 2474–2478.
- [51] T. Reier, D. Teschner, T. Lunkenbein, A. Bergmann, S. Selve, R. Kraehnert, et al., Electrocatalytic oxygen evolution on iridium oxide: uncovering catalyst-substrate interactions and active iridium oxide species, *J. Electrochem. Soc.* 161 (2014) F876–F882.
- [52] S. Cherevko, T. Reier, A.R. Zeradjanin, Z. Pawolek, P. Strasser, K.J.J. Mayrhofer, Stability of nanostructured iridium oxide electrocatalysts during oxygen evolution reaction in acidic environment, *Electrochim. Commun.* 48 (2014) 81–85.
- [53] J. Xu, M. Wang, G. Liu, J. Li, X. Wang, The physical-chemical properties and electrocatalytic performance of iridium oxide in oxygen evolution, *Electrochim. Acta* 56 (2011) 10223–10230.
- [54] D. Chandra, D. Takama, T. Masaki, T. Sato, N. Abe, T. Togashi, et al., Highly efficient electrocatalysis and mechanistic investigation of intermediate IrO_x(OH)_y nanoparticle films for water oxidation, *ACS Catal.* 6 (2016) 3946–3954.
- [55] D.N. Buckley, L.D. Burke, The oxygen electrode. Part 6.-oxygen evolution and corrosion at iridium anodes, *J. Chem. Soc. Faraday Trans. 1* (72) (1976) 2431–2440.
- [56] S. Cherevko, S. Geiger, O. Kasian, A. Mingers, K.J.J. Mayrhofer, Oxygen evolution activity and stability of iridium in acidic media. Part 1. – metallic iridium, *J. Electroanal. Chem.* 773 (2016) 69–78.
- [57] O. Kasian, J.-P. Grote, S. Geiger, S. Cherevko, K.J.J. Mayrhofer, The common intermediates of oxygen evolution and dissolution reactions during water electrolysis on iridium, *Angew. Chem. Int. Ed.* 57 (2018) 2488–2491.
- [58] J.M. Roller, S. Kim, T. Kwak, H. Yu, R. Maric, A study on the effect of selected process parameters in a jet diffusion flame for Pt nanoparticle formation, *J. Mater. Sci.* 52 (2017) 9391–9409.
- [59] J.M. Roller, R. Maric, A study on reactive spray deposition technology processing parameters in the context of Pt nanoparticle formation, *J. Therm. Spray Technol.* 24 (2015) 1529–1541.
- [60] J. Roller, J. Renner, H. Yu, C. Capuano, T. Kwak, Y. Wang, et al., Flame-based processing as a practical approach for manufacturing hydrogen evolution electrodes, *J. Power Sources* 271 (2014) 366–376.
- [61] H. Yu, J.M. Roller, W.E. Mustain, R. Maric, Influence of the ionomer/carbon ratio for low-Pt loading catalyst layer prepared by reactive spray deposition technology, *J. Power Sources* 283 (2015) 84–94.
- [62] L.A. Giannuzzi, B.W. Kempshall, S.M. Schwarz, J.K. Lomness, B.I. Prenitzer, F.A. Stevie, L.A. Giannuzzi, F.A. Stevie (Eds.), *Introduction to Focused Ion Beams: Instrumentation, Theory, Techniques and Practice*, Springer US, Boston, MA, 2005.
- [63] T. Reier, Z. Pawolek, S. Cherevko, M. Bruns, T. Jones, D. Teschner, et al., Molecular insight in structure and activity of highly efficient, low-Ir Ir-Ni oxide catalysts for electrochemical water splitting (OER), *J. Am. Chem. Soc.* 137 (2015) 13031–13040.
- [64] W. Sheng, H.A. Gasteiger, Y. Shao-Horn, Hydrogen oxidation and evolution reaction kinetics on platinum: acid vs alkaline electrolytes, *J. Electrochem. Soc.* 157 (2010) B1529–B1536.
- [65] P.J. Ferreira, G.J. la O', Y. Shao-Horn, D. Morgan, R. Makharria, S. Kocha, et al., Instability of Pt/C electrocatalysts in proton exchange membrane fuel cells: a mechanistic investigation, *J. Electrochem. Soc.* 152 (2005) A2256–A2271.
- [66] C. Massué, V. Pfeifer, X. Huang, J. Noack, A. Tarasov, S. Cap, et al., High-performance supported iridium oxohydroxide water oxidation electrocatalysts, *ChemSusChem* 10 (2017) 1943–1957.
- [67] H. Yu, A. Baricci, A. Bisello, A. Casalegno, L. Guetaz, L. Bonville, et al., Strategies to mitigate Pt dissolution in low Pt loading proton exchange membrane fuel cell: I. A gradient Pt particle size design, *Electrochim. Acta* 247 (2017) 1155–1168.
- [68] T. Pawluk, Y. Hirata, L. Wang, Studies of iridium nanoparticles using density functional theory calculations, *J. Phys. Chem. B* 109 (2005) 20817–20823.
- [69] M.A. Watzky, R.G. Finke, Nanocluster size-control and “magic number” investigations. Experimental tests of the “living-metal polymer” concept and of mechanism-based size-control predictions leading to the syntheses of iridium(0) nanoclusters centering about four sequential magic numbers, *Chem. Mater.* 9 (1997) 3083–3095.
- [70] E.R. Kötz, H. Neff, Anodic iridium oxide films: an UPS study of emerged electrodes, *Surf. Sci.* 160 (1985) 517–530.
- [71] E.M. Davis, C.M. Stafford, K.A. Page, Elucidating water transport mechanisms in nafion thin films, *ACS Macro Lett.* 3 (2014) 1029–1035.
- [72] T.M. Silva, A.M.P. Simões, M.G.S. Ferreira, M. Walls, M. Da Cunha Belo, Electronic structure of iridium oxide films formed in neutral phosphate buffer solution, *J. Electroanal. Chem.* 441 (1998) 5–12.
- [73] M.C. Biesinger, B.P. Payne, L.W.M. Lau, A. Gerson, R.S.C. Smart, X-ray photoelectron spectroscopic chemical state quantification of mixed nickel metal, oxide and hydroxide systems, *Surf. Interface Anal.* 41 (2009) 324–332.
- [74] S.J. Freakley, J. Ruiz-Esquius, D.J. Morgan, The X-ray photoelectron spectra of Ir, IrO₂ and IrCl₃ revisited, *Surf. Interface Anal.* 49 (2017) 794–799.
- [75] J.M. Roller, M.A. Arellano-Jimenez, R. Jain, H. Yu, C.B. Carter, R. Maric, Oxygen evolution during water electrolysis from thin films using bimetallic oxides of Ir-Pt and Ir-Ru, *J. Electrochem. Soc.* 160 (2013) F716–F730.